Hoop and axial plastic buckling modes of submerged cylindrical shells subjected to side-on underwater explosion shock wave

Bingchuan Nie [a],[*], Huiqin Zhang [b],[c],[**]

[a] *School of Physical Science and Engineering, Beijing Jiaotong University, Beijing, 100044, China*
[b] *Key Laboratory for Mechanics in Fluid Solid Coupling Systems, Institute of Mechanics, Chinese Academy of Sciences, Beijing, 100190, China*
[c] *School of Engineering Science, University of Chinese Academy of Sciences, Beijing, 100049, China*

ARTICLE INFO

ABSTRACT

Cylindrical shells are widely used in marine structures from small-sized pipes to various immersed containers and large submarines. Dynamic plastic buckling of the shells could be caused by underwater explosion (UNEX) loads in industrial accidents or hostile attacks. Influential factors including non-dimensional hull shock factor reflecting the resilience of the material to shock intensity, slenderness ratio, localised ring stiffener and endcap are identified. Their impacts on the dynamic buckling modes are discussed relied on the finite element investigations. The results show that the global hoop and axial buckling modes are mainly determined by the hull shock factor and slenderness ratio, respectively. With the increase of hull shock factor, i) back-side buckling, ii) back- and front-side buckling with dominant buckles at the back-side, iii) back- and front-side buckling with dominant buckles at the front side, and iv) overall buckling with very large buckles at the front-side originating from the priority buckling modes can be observed in the circumferential direction. The competition between the front- and back-sides buckling is attributed to their different buckling mechanisms. The former one is caused by shock transmitted from the explosion source through the fluid, whereas the later one is due to striking of the structural hoop stress waves propagated from the front-side via the shell itself. Axial buckling modes consisted of primary and potential buckles alternating in the axial direction could be triggered for a large slenderness ratio, but be concealed by localised buckling modes for small slenderness ratio. The localised buckling modes are controlled by the ring-stiffener and endcap, because they alter the continuity of compression potential of shells.

1. Introduction

Shells are one of the most common elements in marine structures, with their applications ranging from small-sized pipes to various containers and large submarines. Their stability has attracted wide attention over a long period of time. The most significant branch of their application pertains to static buckling and implosion under high hydrostatic pressures, which is an actively pursued area [1–4]. In addition to static buckling, dynamic buckling of shells by transient underwater explosion (UNEX) loads can be caused by industrial

---

accidents or hostile attacks. In general, the dynamic buckling threshold of a shell can exceed its static buckling limit owing to the inertial effect, and an analysis of this phenomenon is very complex, as dynamic stress wave and strain-rate effects are involved.

Several studies have focused on dynamic buckling of typical structural elements subjected to dynamic loads in air. Earlier results for bars, plates, rings, and shells have been well reviewed in monographs [5,6]. In the last decade, numerous investigations aimed at structures of different scales, complex geometries, and complex constitutive behaviours have been conducted. Dynamic buckling of nanostructures [7], composite structures [8], functionally graded structures [9], and viscoelastic structures [10] have been reported. However, the fluid-structure interactions vanish in these cases, and have been confirmed to significantly influence the lower-order buckling modes [11]. Additionally, a few studies have examined the responses of submerged structures to dynamic loads, such as axisymmetric external pressure pulses [12], side-on rectangular incident pressure pulses [13], and intermediate-velocity impacts imposed by airbags [14]. However, their temporal features, including the time duration and temporal decay rate of the time-varying loads, differ significantly from that of UNEX loads.

A UNEX load is a unique dynamic load consisting of a shock phase and a bubble pulsating phase. A quasi-spherical shock with a pressure peak of several MPa and duration of less than one ms is released into water once the detonation of an explosive is accomplished. This shock is then followed by a pulsating bubble load. The duration of the bubble load is several orders of magnitude longer than that of the shock; however, its pressure peak is always less than 20% of the shock's peak. In general, a shock can carry more than half of the energy released by the UNEX. The pressure profile, peak, and impulse of the shock can be estimated by scaling laws proposed half a century ago with surprisingly good precision [15]. These scaling laws are the results of a combination of the theory of propagation of spherical shocks, experimental data, and dimensional analysis. On the other hand, bubble dynamics were captured by the boundary element method [16,17] and smoothed particle hydrodynamic method [18]. Recently, bubble-bubble and bubble-boundary interactions have been reproduced numerically and experimentally [19,20]. Moreover, Geers et al. [21,22] matched the shock and bubble pulsing phases, and provided an entire pressure profile of a UNEX load.

Numerous studies have examined the structural dynamic responses caused by UNEX shocks and bubble loads. Currently, a few high-precision fluid-structure decoupling algorithms are available. Doubly asymptotic approximation (DAA) methods of different orders [23], arbitrary Lagrangian-Eulerian method [24], and others [25–27] have been developed for simulating the nonlinear dynamic responses of structures subjected to UNEX load. The dynamic responses of stiffened plates [28,29], sandwiched plates, cylindrical shells [30,31], stiffened cylindrical shells [32], and composite shells under UNEX shocks have been discussed. Recently, by extending the string-on-foundation method, a simplified model was developed to estimate the response of a deeply immersed cylinder struck by a side-on underwater shock wave, along with a correction factor based on numerical simulations [33]. Additionally, the dynamic responses of plates [16,20] and slender structures with and without fluids inside by the UNEX bubble load have been investigated as well [34,35]. Structures that encounter both shock and bubble loads have also been investigated [36]. Moreover, the response of a hull girder under a load combined with UNEX and surface wave were investigated [37]. Furthermore, several experimental studies have been reported as well [38–40].

In the aforementioned studies relevant to responses caused by UNEX loads, the elastic/plastic deformations and damage to the structure were simulated or measured, and the features of the structural response caused by shock and bubble loads were identified. However, the structural responses were treated without identifying the underlying mechanisms. In fact, by analysing the experimental images and numerical results, at least two different types of structural failure mechanisms can be identified. One is the response dominated by tensile stress, for example, the laceration of plates [28] and dimples between stiffeners of stiffened plates [29]. The other is the dynamic buckling, a typical example of which is the circumferential buckles of a shell [31,38]. The failure of ring stiffeners [32] is also a result of dynamic buckling.

Recently, several studies have investigated the dynamic buckling of shells using axial or side-on underwater shock waves. Bitter and Shepherd [11] measured the deformation of a thin-wall tube subjected to an axial underwater shock wave, generated by a gas gun striking a buffer. Buckling modes 2 and 3 were observed in their experiments. The ratio of the dynamic and static buckling thresholds on a pressure-impulse diagram was presented. Gupta et al. [41] experimentally examined the dynamic buckling of a cylindrical shell subjected to a constant hydrostatic pressure and transient UNEX shock in the axial direction using real-time high-speed digital image correlation deformation measurements. The experiments were conducted at different hydrostatic pressures ranging from 30% to 90% of the static buckling limit with a fixed shock peak. The primary mode, mode-2, was found to be responsible for the collapse; additionally, short-lived higher-order axisymmetric modes were also observed. DeNardo et al. [42] experimentally investigated the buckling of foam-filled double-hull composite cylinders under a combination of hydrostatic and side-on shock loads. They concluded that the foam core could increase the stability and prevent the collapse of the hull cylinder, by activating the vibration response to absorb the energy. As these studies focused on deeply immersed cylinders with high hydrostatic pressures, their focuses were only on the influence of the latter. The buckling modes, and their development and transition were rarely discussed, especially for those caused by side-on UNEX loads.

Overall, there has been a lack of discussion on the dynamic modes of cylindrical shells caused by a side-on UNEX such as a comprehensive identification of influential factors, evolution of buckling modes, and corresponding mechanisms. Moreover, some buckling phenomena in the experiments are not explained thoroughly; for example, severe buckling can occur at the back-side sometimes [38] and at the front-side at other times [31,42]. Motivated by these facts, this study examined the non-dimensional parameters affecting the buckling modes; these are explained in Section 2. The case studies and numerical method employed in this study are described in Sections 3 and 4. Section 5 presents the analyses on hoop and axial dynamic buckling modes of the cylindrical shell investigated, including their development, the role of stress waves on the competition between the buckling at back- and front-sides, as well as the influences of ring stiffener, slenderness ratio, and endcap on the buckling modes. Finally, a summary, along with the conclusions drawn from this study, are presented.

2. Analysis of influential parameters

The dynamic plastic buckling modes of submerged cylindrical shells are affected by four groups of parameters. These are i) the spherical explosion shock: peak pressure p_m, duration θ and explosion standoff S; ii) geometry of the shell: length L, radius R (or diameter D), and thickness δ; iii) structural material properties: density of the material ρ_s, elastic modulus E, Poisson's ratio γ, and yield stress σ_Y; and iv) fluid medium: fluid density ρ_w, speed of sound c (or the modulus of fluid), viscosity μ, and hydrostatic pressure p_s.

We use q to represent each quantity of interest, for example, the length or amplitude of the buckles, which can be expressed as

$$q = f_q(p_m, \theta, S, L, R, \delta, \rho_s, E, \gamma, \sigma_Y, \rho_w, \mu, c, p_s). \tag{1}$$

fourteen independent variables are included in f_q.

By dimensional analysis, Eq. (1) can be transformed into

$$Q = f_Q\left(\frac{\delta}{R}, \frac{L}{D}, \frac{L}{S}, \gamma, T_s, \frac{p_m}{E}, \frac{p_m}{\sigma_Y}, \frac{1}{\mathrm{Re}_g \mathrm{Re}_l}, M_a, Ma_w, \frac{p_s}{p_m}\right). \tag{2}$$

In Eq. (2), T_s, Ma, Re_g, Re_l, and Ma_w can be expressed as

$$T_s = \frac{\theta}{\delta / (E/\rho_s)^{1/2}}, \tag{3a}$$

$$\mathrm{Re}_g = \frac{\rho_w V_g R}{\mu}, \tag{3b}$$

$$\mathrm{Re}_l = \frac{\rho_w V_l R}{\mu}, \tag{3c}$$

$$M_a = \frac{\rho_w R^2 L}{\rho_s \delta R L}, \tag{3d}$$

$$Ma_w = \frac{(p_m/\rho_w)^{1/2}}{c}. \tag{3e}$$

Here, δ/R is the ratio of thickness to radius of the shell; L/D is the slenderness ratio, which can influence the whipping response; and L/S represents the non-uniform effect of the load exerted by the sphere shock along the axial direction of the structure, which can be treated as a planar shock for a non-contact UNEX with a small L/S.

γ, T_s, p_m/E, and p_m/σ_Y are related to the load and structural material. A value of 0.3 is typically assigned to γ and its variation among different metallic materials commonly used in marine structures is insignificant. T_s is the ratio of the time scales of the load to the stress wave propagating through the shell thickness. The impact of T_s on the hoop and axial buckling modes is not apparent as the thickness of the shell is very small, and the propagation of the stress wave in the thickness of the shell would be completed instantaneously (approximately 10^{-5} s), which is much smaller than the duration of the load (approximately 10^{-3} s). p_m/E and p_m/σ_Y both reflect the relationship between the explosion intensity and resilience of the material. In fact, p_m is determined by the intensity of the explosion source and standoff S. This can be quantified by the hull shock actor $W^{1/2}/S$, related to the energy density received at S [43], where W is the weight of the charge in the equivalent TNT. To integrate the resilience of the material, two non-dimensional hull shock factors can be introduced as

$$HSF_E = \frac{\sqrt{W}/S}{\sqrt{E/g}} \tag{4}$$

with focus on the elastic stage from p_m/E, and as

$$HSF_P = \frac{\sqrt{W}/S}{\sqrt{\sigma_Y/g}} \tag{5}$$

with focus on the elastic stage from p_m/σ_Y.

The remaining four dimensionless numbers result from the fluid-structure interactions. In the Reynolds numbers Re_g and Re_l, the velocity scales V_g and V_l can be expressed as

$$V_g = \frac{p_m L R}{\rho_w L R^2} \theta, V_l = R \bigg/ \theta. \tag{6}$$

this implies that V_g and V_l correspond to the velocities of structural global migration and local deformation, respectively. Because the duration of the UNEX shock is extremely small, V_g and V_l are insignificant, implying that large-scale flow separation will not occur, and Re_g and Re_l are dominated by inertia instead of viscosity. M_a, the added mass, is equal to the mass ratio of the fluid displaced by the

structure and structural self-weight. It differs significantly between a shell struck by an air blast and that struck by an underwater explosion. In general, it is approximately equal to unity for underwater floating structures. Ma_w reflects the compressibility of the fluid under shock. It is usually approximately unity for non-contact UNEX because the propagation speed of a UNEX shock in water quickly decays to the acoustic speed [15]. p_s/p_m is the ratio of the hydrostatic pressure to the peak pressure of shock wave. In most marine engineering applications, p_s is significantly less than the pressure of the shock wave. However, it can significantly alter the buckling mode when it falls in the vicinity of the critical hydrostatic pressure of static buckling p_c. Thus, p_s/p_m can be replaced by p_s/p_c.

Based on the above discussion, δ/R, L/D, HSF_P, and p_s/p_c are the four primary governing parameters for the dynamic plastic buckling modes of cylindrical shells subjected to a side-on shock wave. Assuming that the shell is thin and p_s/p_c is small, Eq. (2) can be further simplified as

$$Q \sim f_Q\left(HSF_P, \frac{L}{D}\right)$$

(7)

by dropping δ/R and p_s/p_c.

On the other hand, cylindrical shells are usually strengthened by ring stiffeners and sealed off by endcaps. The two most common localised structures may also affect the buckling modes.

3. Geometry models and study cases

Three cylindrical shell models A, B, and C were examined in this study. They were all made of 6061-T6 aluminium, which has a density of 2784.5 kg/m^3, elastic modulus of 75.6 GPa, and yield stress of 300 MPa. Their geometries are shown in Fig. 1 and are explained below.

(i) Model A is a cylindrical shell with a length and diameter of 1067.0 and 305.0 mm, respectively, with an L/D of 3.2, and is sealed by two end plates. The thicknesses of the shell and the end plates are 6.35 and 25.40 mm, respectively. Model A has the same geometry as the experimental model in Ref. [38]; this would allow a direct comparison.

(ii) Model B, though fundamentally similar to A, has an additional ring stiffener at the middle section; this would allow the influence of the ring stiffener to be examined. The ring stiffener has a rectangular cross-section of height and width of 10.0 and 6.35 mm, respectively.

(iii) Model C has a different L/D and endcaps compared to Model A. Its L/D is approximately 7.0 with a length and diameter of 700 and 100 mm, respectively. We examined this L/D, as it has a low total resistance for the same displaced volume for marine vehicles [44]. The shell thickness of Model C was set to 2.1 mm, which means it would have the same δ/R as Models A and B (approximately 0.042). At the same time, the shell of Model C is sealed by two hemispherical shells, each of thickness 2.1 mm.

To investigate the impact of HSF$_P$, various explosion intensities were exerted on each shell, as listed in Table 1. Cases 1–4 correspond to Model A subjected to charge weights of 27.50–110.00 kg; Cases 5–11 correspond to Model B subjected to charge weights of 27.50–110.00 kg; Cases 11–15 correspond to Model C subjected to charge weights of 8.00–16.00 kg. Cases 16 and 17 has a submerged depth of 100 m. The standoffs for Model A and B are 7.62 m, while that for Model C is 6.00 m. Thus, the ratios of structural length to the corresponding standoff are 0.13–0.14, thus resulting in the same spherical effect of the shock. The HSF$_P$ values for those
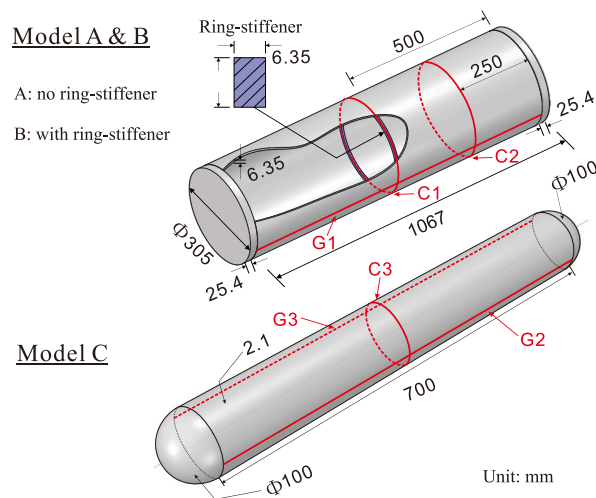

Fig. 1. Schematic of the cylindrical shell models. G1 and G2 are generatrices closest to the charge, and G3 is the generatrix symmetrical with G2 to the axis of the cylindrical shell. C1 and C3 are contours located in the middle cross section, and contour C2 is at a section at quarter length from the end.

Table 1
Parameters for different cases of cylindrical shells subjected to UNEX shock.

Case	Structure model	W (kg)	S (m)	H (m)	σ_Y (MPa)	$\text{HSF}_P \times 10^6$
1	Model A	27.50	7.62	3.66	300	124
2	$L/D = 3.2$	55.00	7.62	3.66	300	176
3	$\delta/R = 0.042$	82.50	7.62	3.66	300	215
4		110.00	7.62	3.66	300	249
5	Model B	27.50	7.62	3.66	300	124
6	$L/D = 3.2$	55.00	7.62	3.66	300	176
7	$\delta/R = 0.042$	68.75	7.62	3.66	300	197
8		82.50	7.62	3.66	300	215
9		90.00	7.62	3.66	300	225
10		96.25	7.62	3.66	300	233
11		110.00	7.62	3.66	300	249
12	Model C	8.00	6.00	3.66	300	85
13	$L/D = 7.0$	10.00	6.00	3.66	300	95
14	$\delta/R = 0.042$	12.00	6.00	3.66	300	104
15		16.00	6.00	3.66	300	120
16		8.00	6.00	100	300	85
17		16.00	6.00	100	300	120

cases are summarised in Table 1.

References [2,45] show that the minor critical hydrostatic pressure of static buckling for perfect cylindrical and spherical shells can be estimated by

$$P_{c,cylinder} = \frac{2E}{1 - 4\gamma^2}\left(\frac{\delta}{R}\right)^3 \tag{8}$$

and

$$P_{c,sphere} = \frac{2E}{\sqrt{3(1 - \gamma^2)}}\left(\frac{\delta}{R}\right)^3 \tag{9}$$

respectively. Accordingly, the critical static buckling hydrostatic pressures are 19.3 MPa for Models A and B, and 6.7 MPa for Model C, which are far above the present hydrostatic pressure, *i.e.*, 0.036 MPa/0.98 MPa at 3.66 m/100 m below the free surface.

4. Numerical method and validation

4.1. Numerical method

Various criteria were specified in the literature for identifying the occurrence of structural dynamic buckling. Generally, they can be divided into geometric, energetic, and failure types [6]. For marine structures under impact, the critical load of dynamic buckling was usually defined as the load at which a small increment can cause sharp variations in the structural deformation [14,28]. The focus of this study is on the structural failure caused by dynamic buckling. Therefore, the dynamic plastic buckling modes of interest are defined as the plastic deformation patterns caused by material compression, which have a different morphology from the initial state, such as plastic dimples or buckles.

The dynamic responses of the shells were investigated using a commercial structural analysis package ABAQUS, based on the finite element method. To integrate the fluid-structure interaction, the water domain surrounding the shell was included in the model. The added mass ratio between the finite and infinite water domain decreased to unity with an increase in the radius ratio of the water domain and shell. Specifically, the added mass ratios were 1.67, 1.13, 1.06, and 1.03 corresponding to radius ratios of 2.0, 4.0, 6.0, and 8.0, respectively. Thus, a radius ratio of 6.0 was adopted in for all the cases to capture the influence of fluid without a heavy computational expense.

The shell was free to move, and was discretised using 4-noded quadrilateral shell elements (S4R). More than ten mesh sizes were assigned for the shortest wavelength estimated by the product of the speed of sound (~5200 m/s) and duration of the shock wave (~0.5 ms). The water domain was discretised using 8-noded, structure elements (AC3D8R). The meshes of the water domain allowed for larger sizes than the structure because acoustic waves propagate slower in water than in solids. The pressure and displacement of the structure and fluid were coupled at the fluid-structure interface. The acoustic element of the water domain was updated to follow the shell surface in every iteration, where each fluid node was an average of the nearby nodes of the shell. The radiation boundary condition was adopted for the exterior boundaries of the water domain, and this allowed the shock to pass through without being reflected back into the computational domain.

The Johnson-Cook damage model was adopted for the yield stress. The fluid was assumed to be inviscid, but compressible, with a bulk modulus of 2.14 GPa. Water was capable of undergoing cavitation by allowing an arbitrarily large volume expansion without further drop in pressure once the pressure is lower than the cavitation pressure limit.
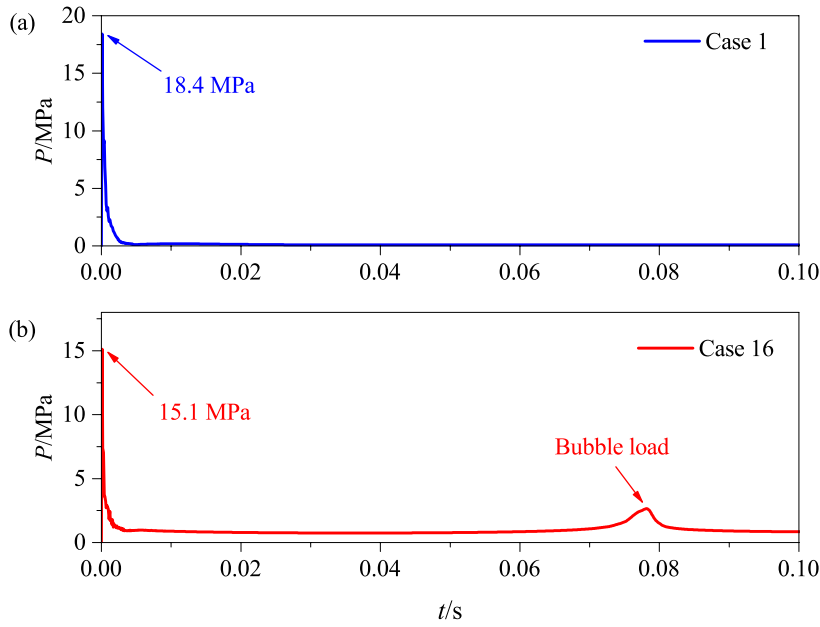
Fig. 2. Pressure profiles monitored at 2.5 cm near the shell in Cases 1 and 16.

The UNEX load was assumed to be spherical, and it comprised a shock phase ($t < T_c$) and bubble oscillation phase ($t \geq T_c$). The historical profile of pressure at S for the shock and bubble oscillation phases can be expressed as [21]:

$$P(S,t) = \begin{cases} \dfrac{\rho_w}{4\pi S}\left(\dfrac{a_c}{S}\right)^A \ddot{V}\left([a_c/S]^B t\right), t < 7T_c \\ \rho_w a^2 \dfrac{\ddot{a}+2a\dot{a}^2}{S}, t \geq 7T_c. \end{cases} \tag{10}$$

The bubble radius a can be estimated using the doubly asymptotic approximation model [25], which was solved using a fourth-order Runge-Kutta integration method.

The volume acceleration is expressed as

$$\ddot{V}(t) = \frac{4\pi a_c}{\rho_w}P_c\left[0.8251\exp\left(-1.338\frac{t}{T_c}\right) + 0.1749\exp\left(-0.1805\frac{t}{T_c}\right)\right]. \tag{11}$$

Here, a_c is the radius of the explosive charge and T_c equals a_c/v_c. The constants P_c, v_c, A, and B are constants related to the charge material, and the value of them are 1.71, 1.47, 0.15, and 0.29, respectively, for HBX-1 of density 1.72 g/cc. In practice, the explosion source was located outside the fluid domain and the UNEX load, calculated using Eqs. (10) and (11), was imposed as an initial pressure field in the water domain at the moment when the shock front propagated to a reference point in the water domain near the shell.

The time history of pressure was monitored for each case, and those for Cases 1 and 16 are plotted in Fig. 2. The distance between the monitor probe and explosion source is 7.44 m in Case 1 and 5.93 m in Case 16. In either case, the probe is located 2.5 cm from the shell wall. As the bubble radius in Case 1 is 4.2 m according to the expression $3.36W^{1/3}/(H+10.3)^{1/3}$ [15], which is much larger than the explosion depth, the explosion bubble is vented out at the surface. Therefore, a pulse generated by the bubble is not observed, as shown in Fig. 2(a). The hydrostatic pressure is not apparent because H is only 3.66 m. In Case 16, the pressure at the probe increases to 15.1 MPa, and then decreases to the hydrostatic pressure quickly, followed by a pulse at 80 ms due to the bubble collapse (see Fig. 2 (b)). Based on the expression $52.16\,(W^{1/3}/S)^{1.13}$ [15], the pressure peaks at the probe in Cases 1 and 16 are 18.8 and 15.3 MPa, respectively. This result agree with the peaks of the UNEX shock in the two simulations. No significant cavitation is detected by the probes near the shell.

4.2. Validation

Case 1 was examined experimentally by Kwon and Fox [38], in which the hoop and axial strains at the middle section and near the endcap were measured using strain gauges. To validate the aforementioned numerical method, Case 1 was simulated with strains at B1, B2, B3, and C1 monitored, as shown in Fig. 3. B1, B2, and B3 is located on the circumference of the middle cross-section and are the nearest, uppermost, and farthest points on the shell from the explosion source, respectively. The shell is surrounded by water with a radius ratio between the water domain and shell of six. Two structured grids, an intermediate mesh and a denser mesh, with different spacings were used for the mesh independence study. In the intermediate mesh, 5736 S4R and 327,860 AC3D8R elements were used
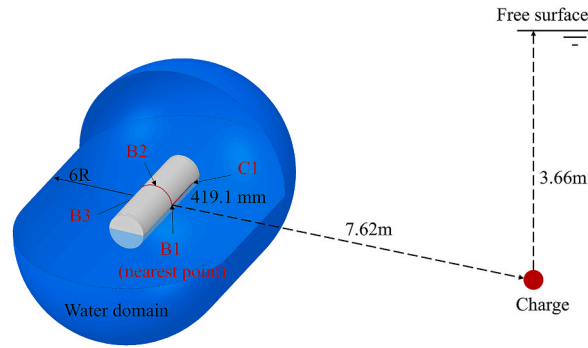
Fig. 3. Schematic diagram of the arrangement and positions of the probes.

for the shell and water domains, respectively. On the other hand, 12,736 S4R and 627,860 AC3D8R elements were used for these domains in the denser mesh. An almost uniform grid spacing was adopted for the shell; however, a non-uniform grid spacing was used for the water domain with the finer grid being used in the proximity of the shell.

The numerical results of the intermediate and denser meshes in our study were compared with the numerical and experimental data from Ref. [38]. The dots in Fig. 4(a) representing the experimental results indicate that region B1 underwent oscillations of the axial strain with a slight compression. The negative hoop strain in Fig. 4(b) reflects the severe compression in the circumferential direction. Our numerical results at B1 confirm these features and the predicted final strains are in good agreement with the experimental results. However, the first peaks of both the axial and hoop strains are underestimated in the numerical simulations, as shown in Fig. 4(a). Fig. 4(c–f) show that the numerical results capture the initial magnitudes and final strains satisfactorily. The hoop strain at B3 is presented in Fig. 4(g), and significant discrepancies are observed in this variable between the experiments and numerical simulations. However, the axial strain at B3 is not provided because the corresponding strain gauge failed during the experiment. As for the temporal features, the peaks of the strains in the simulations are all present earlier than those in the experiments, which is acceptable considering that it was difficult to determine the initial time in the experiments. The dominant oscillating frequency corresponding to the ringing phenomenon could be identified in the numerical results. However, the oscillation frequency is higher than that in the experiments. This is because the strain gauge output was filtered at 2000 Hz in Ref. [38], and the shell constraints in the experiments and simulations are slightly different from each other. The insignificant difference between the results of the intermediate mesh and those of the denser mesh confirms that the results are mesh-size-independent. By comparing the numerical results in this study with those from Ref. [38], it is observed that the improvement in the predictions for strain is clear in our simulations, especially for the axial strain at B1, and hoop strains at C1 and B3.

5. Plastic deformation and buckling modes

5.1. Dynamic buckling of model A

(1) Dynamic responses and failure regions

The dynamic responses of Case 1 are shown in Fig. 5. The primary response is global migration away from the charge, which would not contribute to a structural deformation. Another one is the whipping response as illustrated by the bending curvatures at time instances of 0.3 and 1.2 ms. As the duration of shock is very short, whipping response by shock is usually of secondary importance [35]. The third one is the local structural response caused by the propagating stress waves. At 0.6 ms, two dominant stress waves are generated near the end plates. These two waves propagate towards the middle cross-section (arrows at 0.9 ms), strike at the middle cross-section (arrow at 1.2 ms), and finally propagate towards the opposite end plate (arrow at 1.5 ms). Because the axially propagated stress waves are quite complex, these two waves became unclear at 1.8 ms. In addition to the stress waves propagating along the axial direction, stress waves propagating along the hoop direction also exist.

The plastic regions of Case 1 are identified by the equivalent plastic strain, as shown in Fig. 6(a) and (b). The same for Case 4 is also presented for a comparative observation of the influence of HSF_P (see Fig. 6(c) and (d)). Fig. 6(a) and (b) show that there are three main plastic regions, namely I, II, and III. Only regions I and III are discussed hereafter due to their symmetry. However, Fig. 6(c) and (d) show that the whole shell yielded for large HSF_P, and the most severe plastic deformation at the front-side are located in regions IV and I. Upon comparing Cases 1 and 4, it appears that the thresholds of plastic deformation for regions I and III are lower than that of region IV. However, region IV tends to have a larger plastic deformation than regions I and III for a large HSF_P. In other words, the growth rate of plastic deformation in region IV is larger than that in regions I and III with a higher HSF_P; this implies different deformation mechanisms in those regions. Furthermore, the plastic deformation of the region above (region V) and the symmetric deformation below are significant as well.
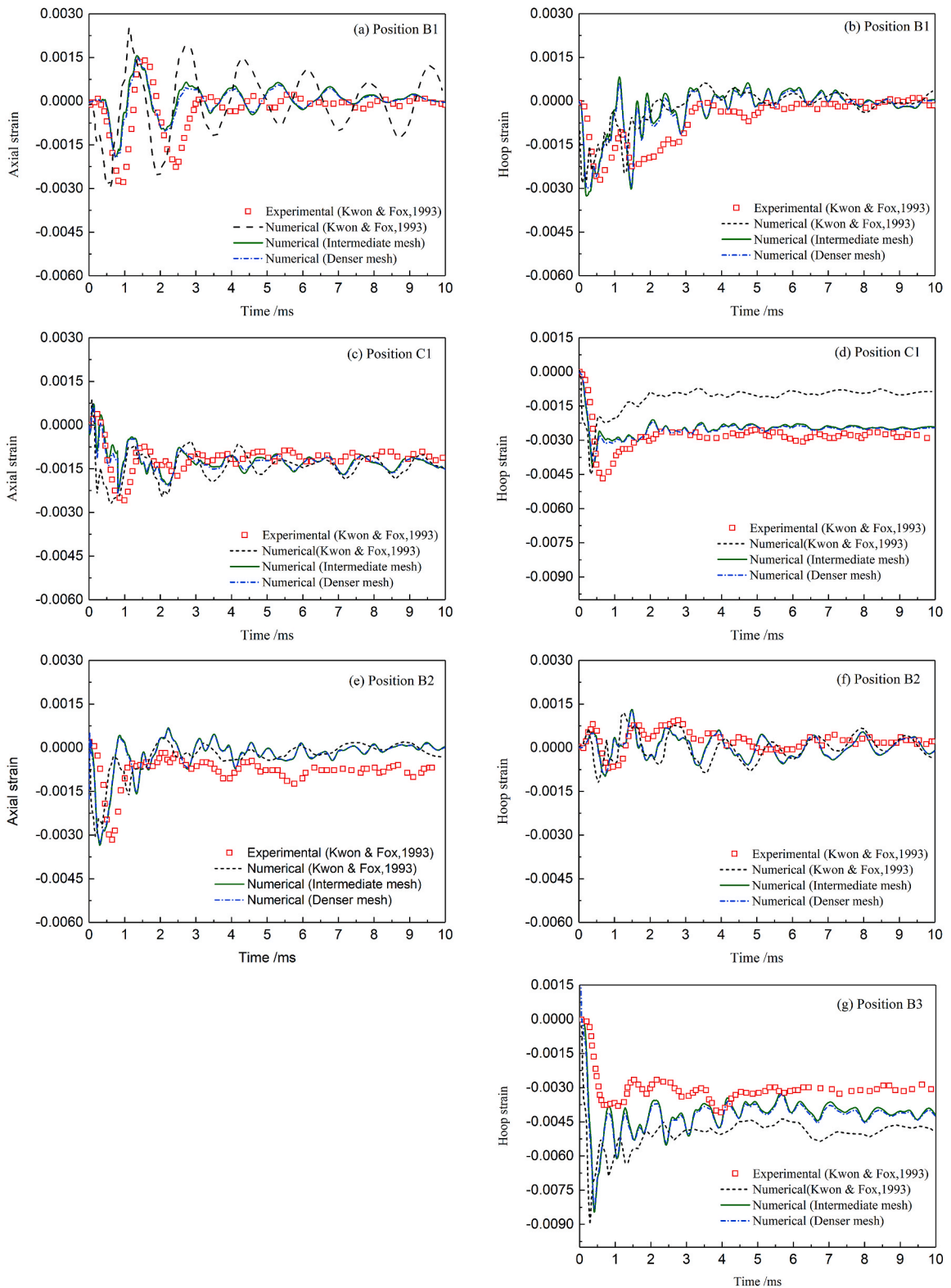
(2) Axial buckling modes

Fig. 4. Time histories of axial (left) and hoop (right) strains at four typical positions: (a and b) at B1; (c and d) at C1; (e and f) at B2; (g) at B3 (see Fig. 3). The solid lines represent the numerical results from this study, while the dotted and dashed lines represent the experimental and numerical results, respectively from Ref. [38]. The comparison of the axial strain at position B3 could not be presented as the corresponding strain gage failed in the experiment.
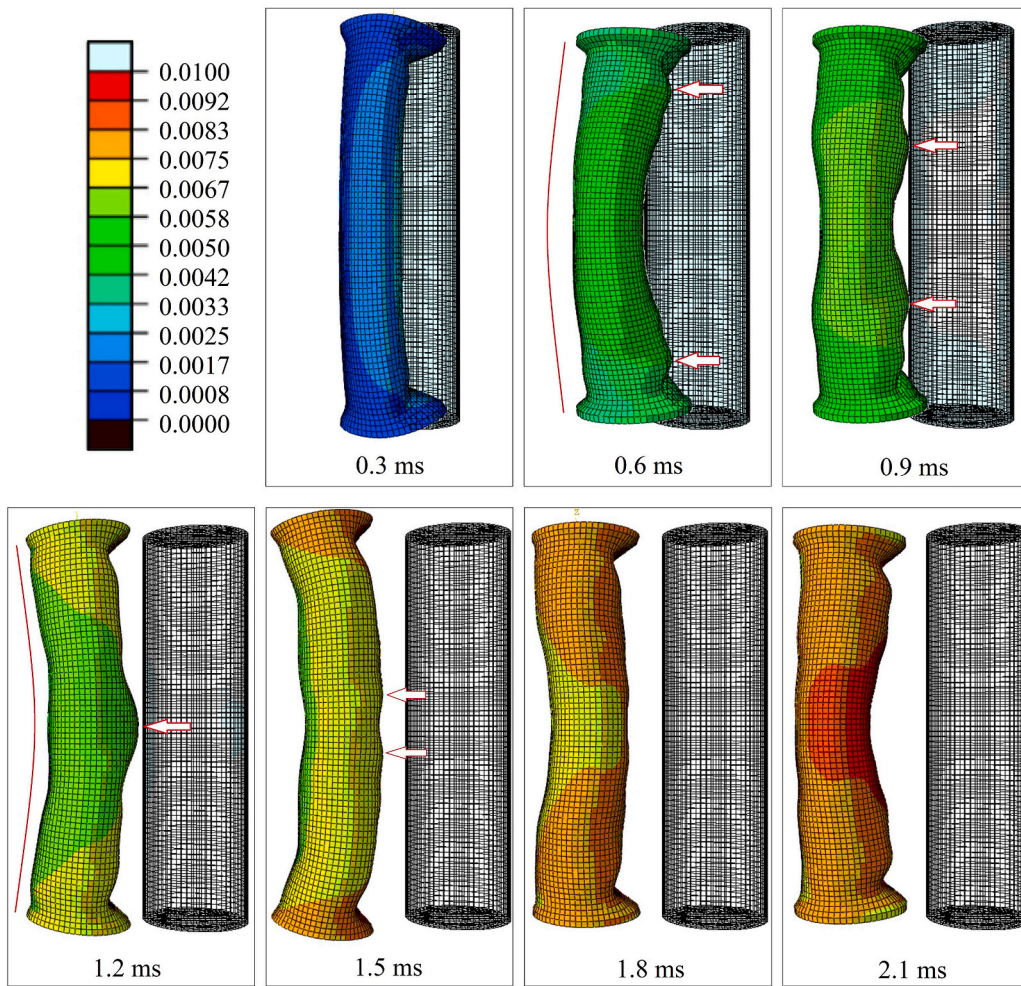
Fig. 5. Displacement and deformation (m) of shell Model A in Case 1. The initial position of the shell is sketched by the grid lines. To illustrate the response clearly, the displacements (contour plots) of the shell have been enlarged 50X.

The hoop and axial plastic strains along G1 (see Fig. 1) of Case 1 are plotted for five instances during the initial 0.7 ms, as the plastic deformation occurs only during this period. Fig. 7 shows that the maximum magnitude of the plastic hoop strain due to compression is almost double that of the plastic axial strain due to tension, which implies that the failure of region I is caused by dynamic buckling. According to the axial plastic strain, region I can be further divided into three sub-regions, namely a tension region I-0 near the end plate, and two compression regions I-1 and I-2. In sub-region I-0, the hoop compression is superior to axial tension, whereas both hoop and axial compressions occur in regions I-1 and I-2. The development of the axial plastic strain also demonstrates that dynamic buckling mainly occurs in sub-regions I-1 and I-2 during 0.2–0.3 ms. It is noteworthy that a region with a potentially positive axial plastic strain could appear between I-1 and I-2.

The development of elastoplastic strains in Case 1 along G1 is plotted in Fig. 8. Fig. 8(a) shows that the hoop strain is almost uniform along G1 at 0.15 ms except for a slightly larger strain near the end plate. Then, the deviation between the strain at the ends (region I) and that in the middle (region IV) increased remarkably with time. As the end plate is harder to compress circumferentially than the shell, it results in an inhomogeneous resilience to hoop compression along G1; furthermore, a strong axial tension occurs in sub-region I-0, corresponding to the peaks near the end plate, as shown in Fig. 8(b). Later, the reverse rotation motion of the end plates due to the asymmetric tension at the front- and back-sides of the shell become notable, which led to the axial compression of the front side, that is, the two peaks of the hoop total strain near the end wall, as presented in Fig. 8(a). Fig. 8(b) clearly shows the generation of wave patterns along G1 due to the axial compression. When the strains of these wave patterns exceed the yield stress, plastic buckles, such as those in sub-regions I-1 and I-2, could be observed. In Case 1, the axial strain in the middle region is small and the material remains elastic, as shown in Fig. 7. Therefore, we can infer that buckling in region I is caused by the end plate.

The effect of HSF_p on the final plastic strains of shell model A is presented in Fig. 9. It indicates that the hoop plastic compression strain is larger than the axial plastic tension strain in region I-0 for Case 1, with an HSF_p of 124×10^{-6}. When HSF_p increases to 249×10^{-6}, the maximum axial and hoop plastic strains near the endplate are both approximately 0.2. In other words, the axial plastic
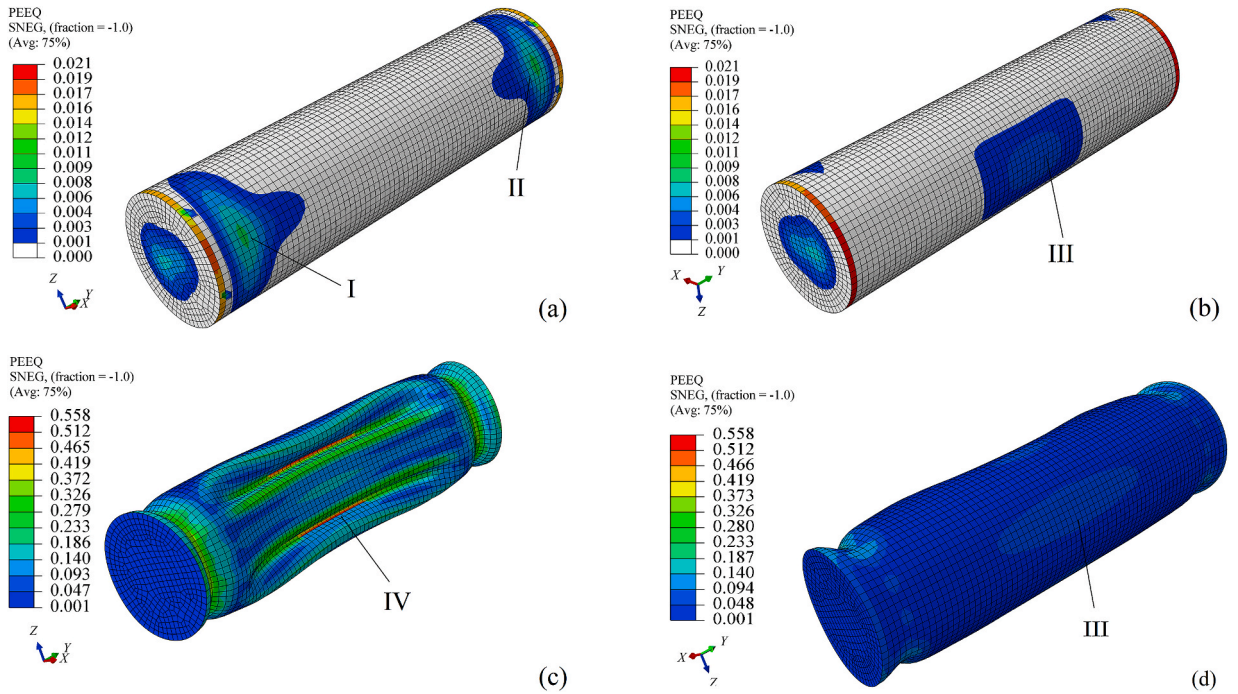
Fig. 6. Equivalent plastic strain for Cases 1 and 4: (a) and (b) front- and back-sides, respectively for Case 1; (c) and (d) front- and back-sides, respectively for Case 4. The front-sides are the sides facing the explosion source.
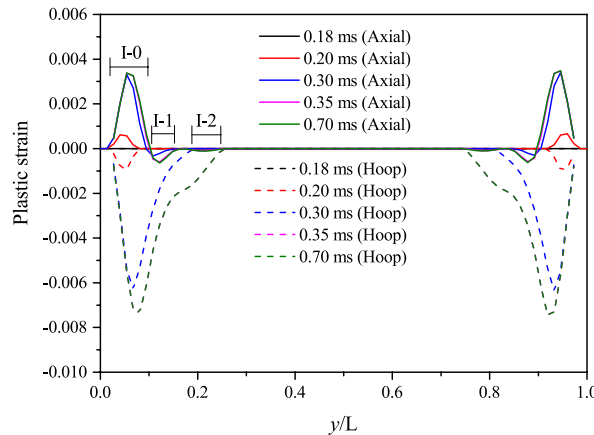

Fig. 7. Evolution of hoop (dashed lines) and axial (solid lines) plastic strains along G1 of Case 1. The horizontal axis displays the non-dimensional length along the axis of the structure. The plastic hoop strain curves at 0.35 and 0.70 ms are almost identical.

tension strain catches up with the hoop plastic compression strain. This implies that the failure in region I-0 could be caused by tension rather than by buckling for large HSF_p values. However, buckling always dominate in the region beyond I-0 because the hoop plastic compression strain is always larger than the axial tension strain. In general, the buckling area increase with HSF_p; however, the number of axial buckles near the end plate is insensitive to HSF_p.

(3) Hoop buckling modes

The development of plastic strain along contour C1 in Fig. 10 demonstrates that the back-side (region III) is in a compression state in the hoop and a tension state in the axial direction. The magnitude of the compressive strain is almost double that of the tensile strain. Therefore, the failure in region III is dominated by hoop buckling with three typical buckles (III-1, III-2, and III-3).

The development of total hoop strain along C1 during 0–0.3 ms with an interval of 0.01 ms is presented in Fig. 11. It shows that the development of plastic deformation along the circumference of the shell could be divided into three phases, that is, 0–0.1 ms, 0.1–0.18
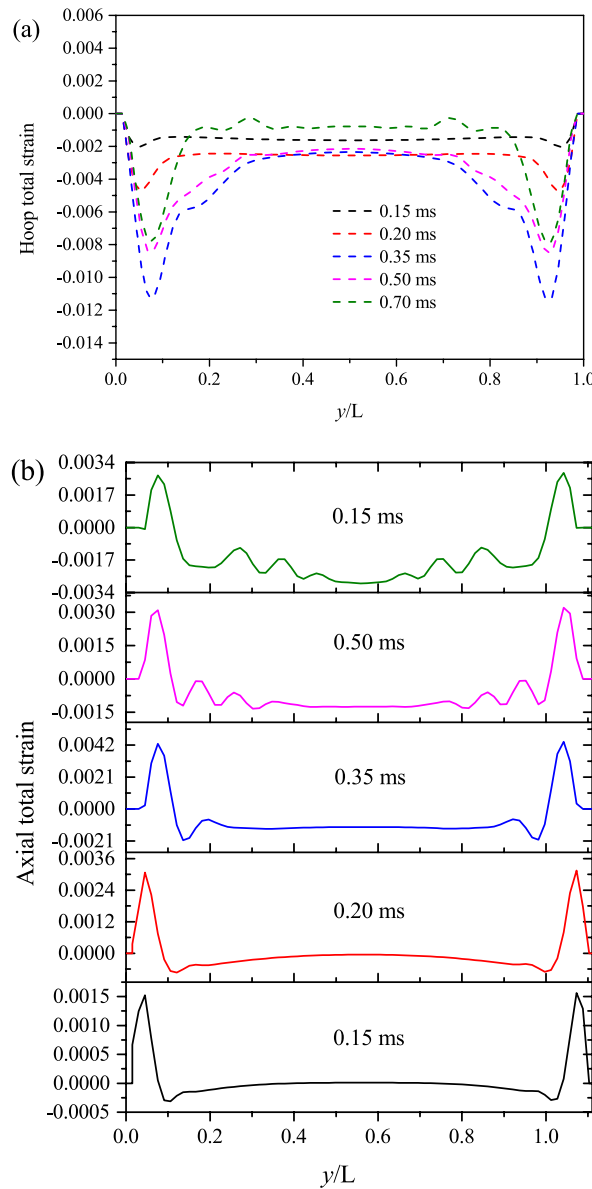
Fig. 8. Evolution of total (elastoplastic) strains along G1 of Case 1: (a) hoop strain; (b) axial strain.

ms and 0.18–0.3 ms. During the first phase (0–0.1 ms), an elastic hoop strain occurs at the front side, once the shock strikes the shell; then, the elastic strain region expands to cover the entire circumference. In the second phase (0.1–0.18 ms), the elastic hoop strain at C1 increases globally. After 0.18 ms (third phase), the increase in the hoop strain at the front-side corresponding to the region around 0/360° in Fig. 11(a) stops. Three peaks of strain appear at the back-side and continue to grow. Furthermore, the growth of the two peaks by the side stop at 0.3 ms, and the peak at the middle increases until 0.4 ms (see Fig. 10). In other words, a stress wave is generated at the nearest point of the shell when the shock strikes the shell; then, two waves form at the top and bottom, propagating along the circumferential direction. The superposition of these two stress waves results in three peaks of strain at the back-side. In fact, the generation of the three plastic buckles III-1, III-2, and III-3 is not influenced by the fluid-shell interaction. The propagating speed of the stress wave in the shell is much larger than that in water; for additional information, readers may refer to the experimental observations in Ref. [46]. In addition, the plastic strains during 0.23–0.30 ms with the 0.01 ms interval are also presented in Fig. 11(b). It shows that the plastic strain starts during 0.27–0.28 ms. The magnitude of the plastic strain in III-2 is always larger than that in III-1 or III-3; this implies that a potential bucking mode with only one plastic buckle exist when the threshold for the occurrence of plastic deformation falls between the plastic strains in sub-regions III-1 and III-2.

For comparison, the development of the total hoop strain along C1 in Case 4 is presented in Fig. 12, which shows that the hoop strain along C1 could be divided into three phases. The first two phases would be very similar to those of Case 1, as shown in Fig. 11(a).
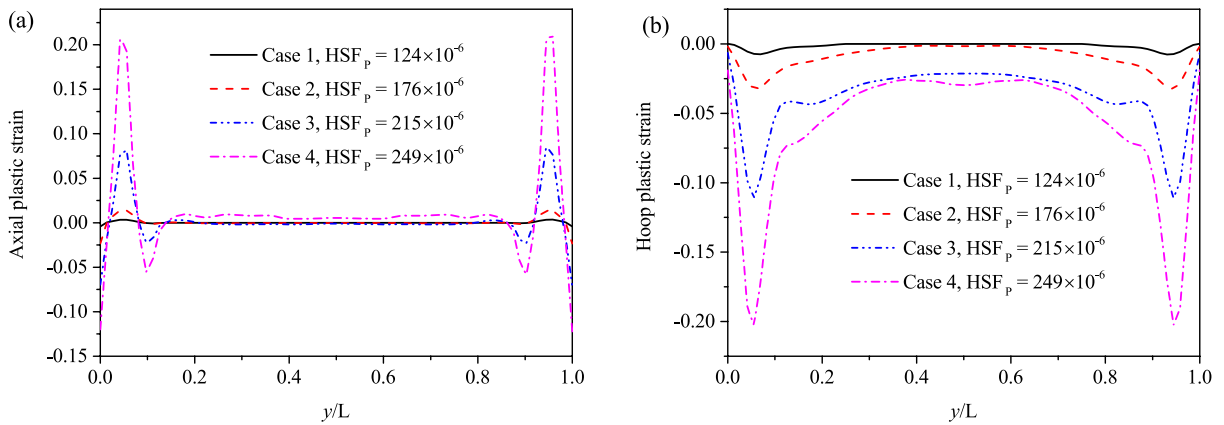
Fig. 9. Effect of HSF$_P$ on axial buckling modes, plotted along G1: (a) final axial plastic strain; (b) final hoop plastic strain.
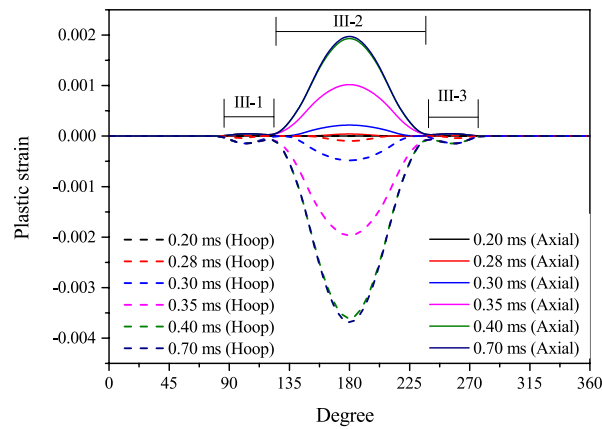

Fig. 10. Hoop (dashed lines) and axial (solid lines) plastic strains along contour C1 of Case 1. The horizontal axis represents degrees, with zero corresponding to the nearest point of the shell to the explosion source.
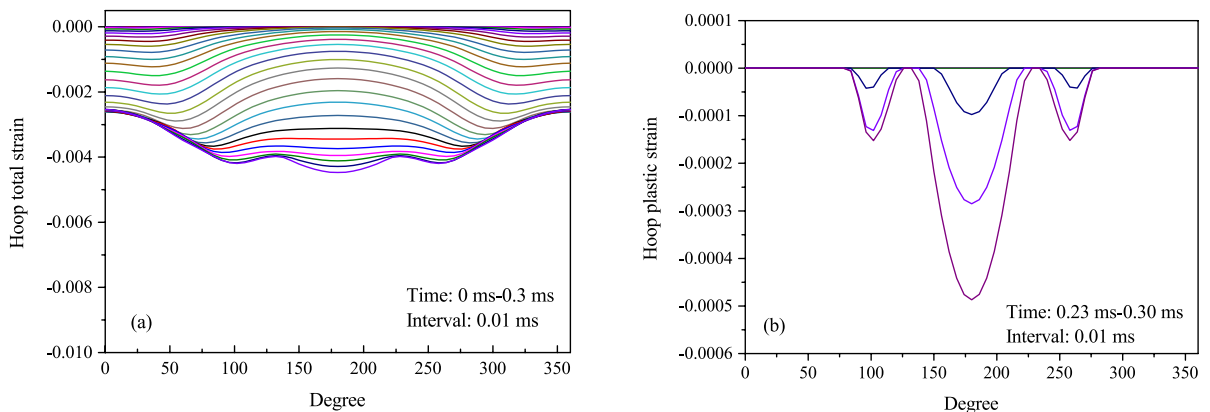

Fig. 11. Evolution of hoop strain on contour C1 (see Fig. 3) of Case 1. The horizontal axis represents degrees, with zero degree being the point nearest to the charge: (a) total (elastoplastic) hoop strain; (b) hoop plastic strain.

However, the strain at the front-side continue to increase at a large growth rate instead of stopping the increase in the third phase. This is because HSF$_p$ in Case 4 is large enough to cause buckling at the front-side at 0.24 ms (see Fig. 11(b)). Moreover, three buckles, III-1, III-2, and III-3, at the back-side are not observed in Case 4 (see Fig. 12(b)); this is because the buckling at the front-side consumes the energy of the stress waves, which therefore could not cause buckling at the back-side. Therefore, the buckling mechanisms at the front-
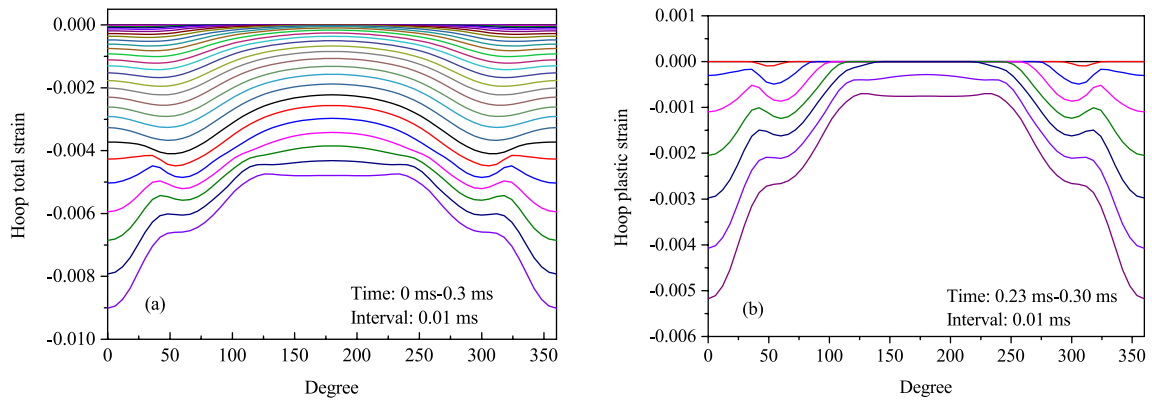
Fig. 12. Evolution of the hoop strain along contour C1 (see Fig. 3) of Case 4. The horizontal axis represents degrees, with zero degree being the point nearest to the charge: (a) total (elastoplastic) hoop strain; (b) plastic hoop strain.

and back-sides were different. More specifically, the buckling at the back-side resulted from the striking of the structural hoop stress waves, whereas the front-side buckling is due to the shock transmitted from the fluid.

The final hoop and axial plastic strains along contour C1 for Cases 1–4 are presented in Fig. 13, from which the 'competition' between the buckling at the back- and front-sides with an increase in HSF$_p$ is very clear; that is, the buckling at the back-side occurred more easily, as shown in Fig. 13(a) and (b), because it is caused by the superposition of the two stress waves generated at the front side. However, the growth rate of the buckling at the front-side become much larger with an increase in HSF$_p$; thus, the amplitude of the plastic deformation at the front-side finally catches up with, and even exceed that of the back-side buckling. Thus, a very large plastic hoop strain can be observed in the regions around 45 and 315° in Cases 3 and 4, as shown in Fig. 13(c) and (d).

5.2. Dynamic buckling of model B

(1) Failure regions

Comparing the dynamic responses of Models B and A, it is difficult to observe the influence of the ring stiffener on the global migration and whipping response. However, the ring stiffener could significantly change the local behaviour of the region nearby, and inhibit the hoop plastic deformation of the shell, overall, as shown in Fig. 14. More specifically, the plastic regions of Case 1 in Fig. 6 and Case 5 in Fig. 14 show that plastic region III is divided into two sub-regions by the ring stiffener; the maximum plastic strain in region IV of Case 11 is reduced by approximately 25% compared with that of Case 4, and the impact of the ring stiffener on plastic regions I and II is not clearly apparent.

(2) Buckling modes

Fig. 15 shows that the hoop plastic strain appears prior to the axial plastic strain with an increase in HSF$_p$, and the axial plastic strain at y/L from 0.1 to 0.9 could only be observed for Cases 8–11. Fig. 15(b) shows that the shell was compressed in the hoop direction for every cross-section. Four peaks symmetrical about the ring stiffener at $y/L = 0.3$, 0.42, 0.58, and 0.7 exist for Case 11, with the former two marked as P11-1 and P11-2. The axial plastic strains at P11-1 and P11-2 are also negligible, which confirms that buckling dominated the structural deformation. Notably, buckling is not observed at P11-1 for Case 8. In other words, the buckling modes are altered when HSF$_p$ increases from 215 to 249. Buckles P11-1 and P11-2 are not observed in Fig. 9. This means that the ring stiffener could change the axial buckling mode, as it influences the equivalent slenderness ratio between sections harder to compress circumferentially.

The axial and hoop plastic strains along contour C2 are shown in Fig. 16. The magnitude of the hoop compression strain is always larger than that of the axial tension strain, indicating that buckling is dominated the plastic deformation on contour C2. Fig. 16 shows four types of hoop buckling modes similar to those of Model A in Fig. 13. These were: i) weak plastic buckling at the back-side and almost no buckling at the front side (see Fig. 13(a)), ii) weak plastic buckling at both back- and front-sides (see Fig. 13(b)), iii) weak plastic buckling at the back-side and severe plastic buckling at the front side (see Fig. 13(c)), and iv) priority buckling modes at the front side, which grow into very large buckles (see Fig. 13(d)). In other words, the ring stiffener has a minor impact on the hoop buckling modes, except for the cross-section close to the ring stiffener; however, it could significantly mitigate the magnitude of buckling.

The plastic regions of the ring stiffener were also examined. When HSF$_p$ is small, the ring stiffeners in Cases 5–7 remain elastic, as shown in Fig. 17(a). One, two, and four buckling regions (Fig. 16(b), (c), and (d), respectively) can be observed with an increase in HSF$_p$. When HSF$_p$ increases further, the four buckling regions expand to contact one another, resulting in the yielding of the entire ring stiffener. Fig. 17(b) and (c) indicate that the buckling threshold at the back-side is larger than that at the front side. Comparing this with the hoop buckling mode of the shell suggests that the resilience of the ring stiffener at the back-side to tangential compression is
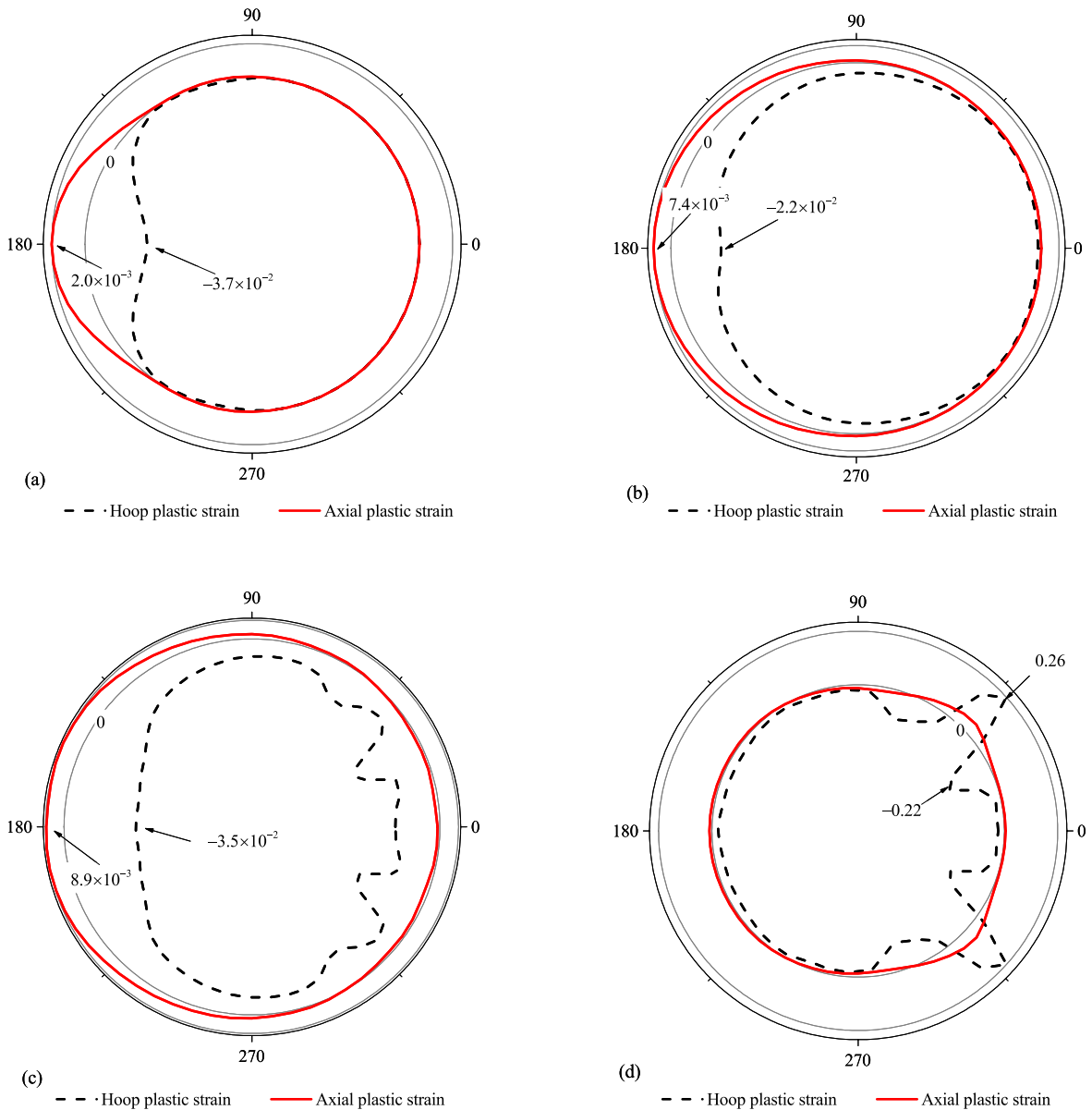
Fig. 13. Final hoop (dashed line) and axial (solid line) plastic strains along contour C1 of Model A; (a), (b), (c), and (d) correspond to Cases 1–4, respectively; the minimum and maximum values of the plastic strains are marked.

improved significantly due to the much larger thickness.

5.3. Dynamic buckling of model C

Fig. 18 presents the failure regions of shell Model C subjected to a shallow UNEX. It indicates that the equivalent plastic strain is symmetrical about the middle cross-section of the shell; therefore, only one half of the shell is discussed hereafter. Along the axial direction, cross-section D has the largest equivalent plastic strain, whereas cross-sections A, B, and C tend to exhibit severe plastic deformation as well. The insignificant difference between cross-sections A and B suggests that the influence of the hemispherical shell on the axial and hoop buckling is localised. For the hoop buckling modes, the competition between the back-side and front-side buckling is clear; that is, the back- and front-side exhibit dominant buckles at the back-side, as can be seen in Fig. 18(a); however, overall buckling with very large buckles at the front-side can be seen in Fig. 18(d).

To clearly address the buckles along the axial direction, the displacements and strains along G2 and G3 of Case 14 are plotted in Fig. 19 as an example. The difference between the displacements of G2 and G3, that is, the grey band in Fig. 19(a), indicates that the majority of the shell is compressed by shock, except for the two ends joining the hemispherical shells. In the compression regions, seven
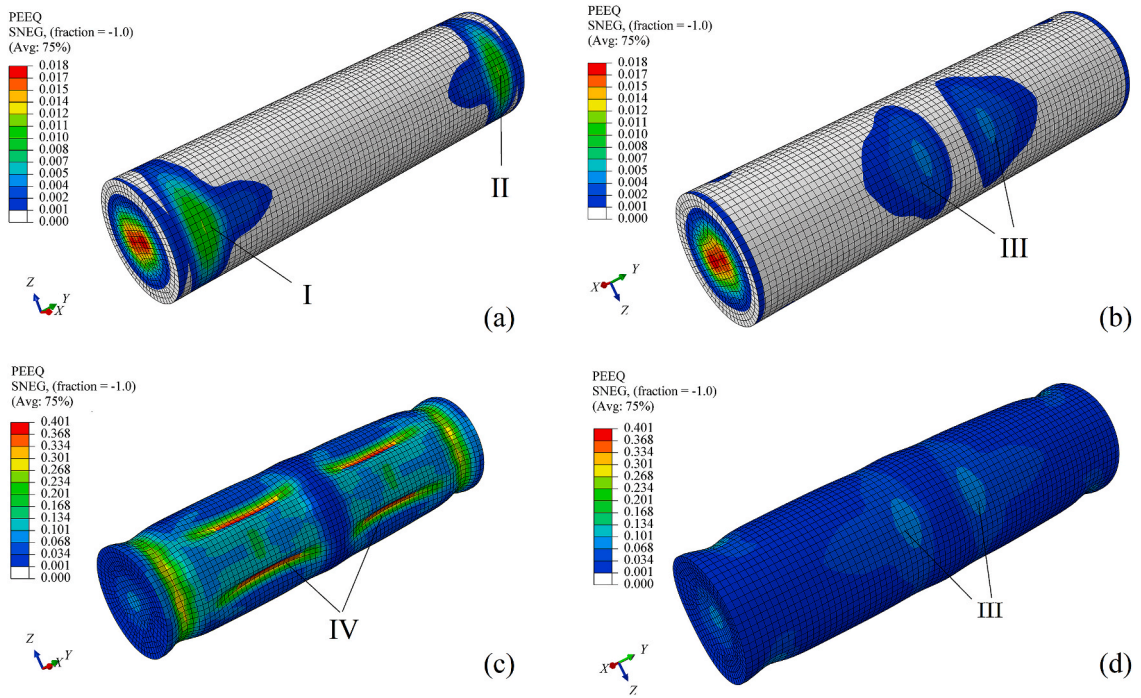
Fig. 14. Equivalent plastic strains of Cases 5 and 11; (a) and (b) front- and back-sides of Case 5, respectively; (c) and (d) front- and back-sides of Case 11, respectively.
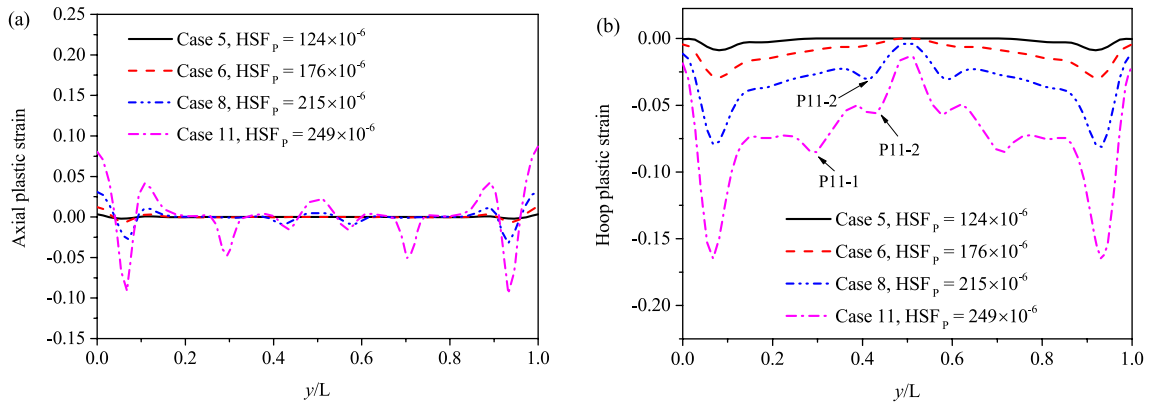

Fig. 15. Influence of HSF$_P$ on plastic strains along G1 of Model B: (a) axial strain; (b) hoop strain.

primary extrema along the axial direction are very clear, that is those at $y/L = 0.945, 0.835, 0.665$, and 0.5, and the symmetrical ones. These extrema are more evident in the plastic strain curves, as can be seen in Fig. 19(b). In addition to the seven primary extrema, four secondary extrema marked by arrows can also be identified in Fig. 19(b). In addition, Fig. 19 shows that the influence of the hemispherical shell is limited to the nearby region.

Comparing the axial buckling modes of Models A and C depicted in Figs. 9 and 19, respectively, it can be observed that global axial buckling modes with uniform spacing between the buckles are generated in Model C, but not in Model A. This is because the localised axial modes caused by the endplate or stiffener of Model A covered the entire shell, resulting in no space for the development of global axial buckling modes. Thus, L/D may have a significant effect on the axial buckling modes.

Fig. 20 presents the plastic hoop strain along contour C3. It confirms that the competition between the back- and front-sides buckling is independent of L/D. Fig. 20 also indicates that the hoop buckling mode is symmetrical about the $180°$-plane, and the difference between Cases 15 and 17 (or Cases 12 and 16) is not apparent; that is, the bubble load and hydrostatic pressure do not influence the hoop buckling mode, as both are much less than the magnitude of shock or critical hydrostatic buckling pressure.

Fig. 21 presents the total axial and hoop strains at the nearest point versus time. This figure shows that the bubble load has caused an evident hoop and axial strain; however, they remain in the elastic stage. According to Fig. 20(a), the impact of the hydrostatic
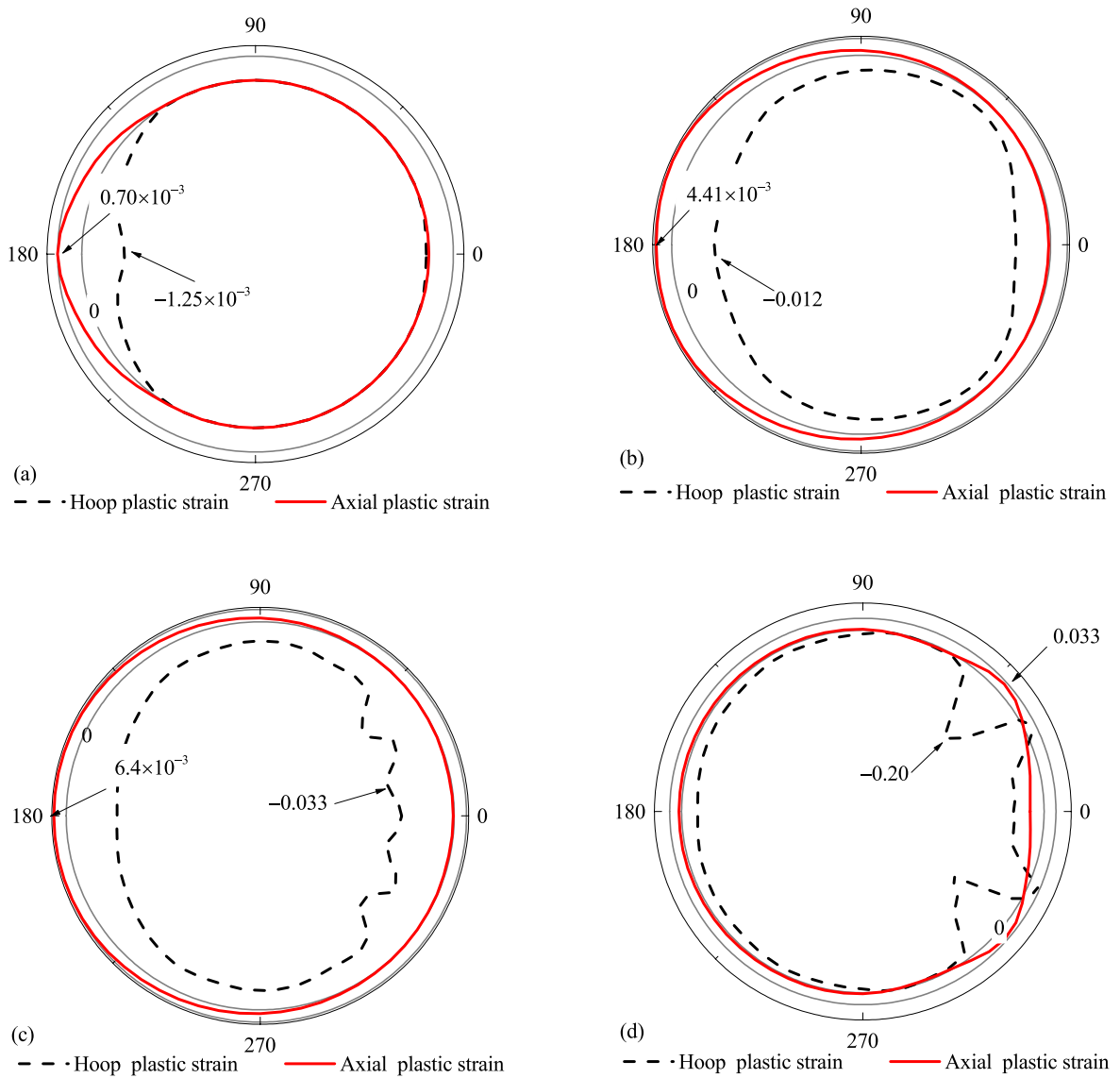
Fig. 16. Final hoop (dashed line) and axial (solid line) plastic strains along contour C2; (a)–(d) correspond to Cases 5, 6, 8 and 11, respectively.
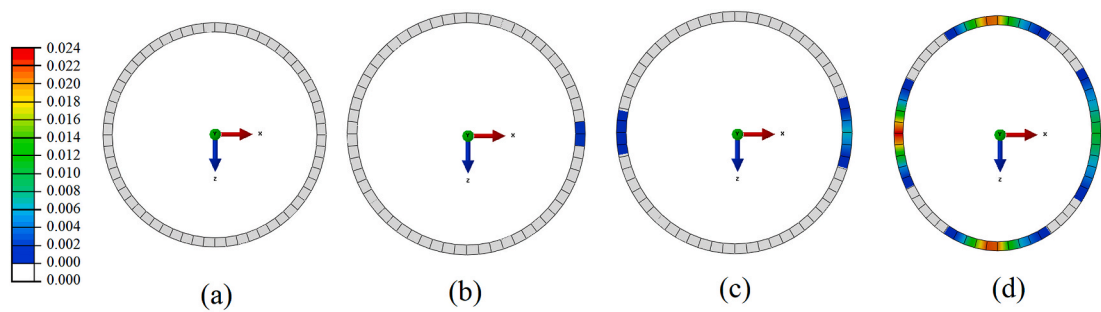

Fig. 17. Equivalent plastic strain of the ring stiffener; (a)–(d) correspond to Cases 7–10, in that order.
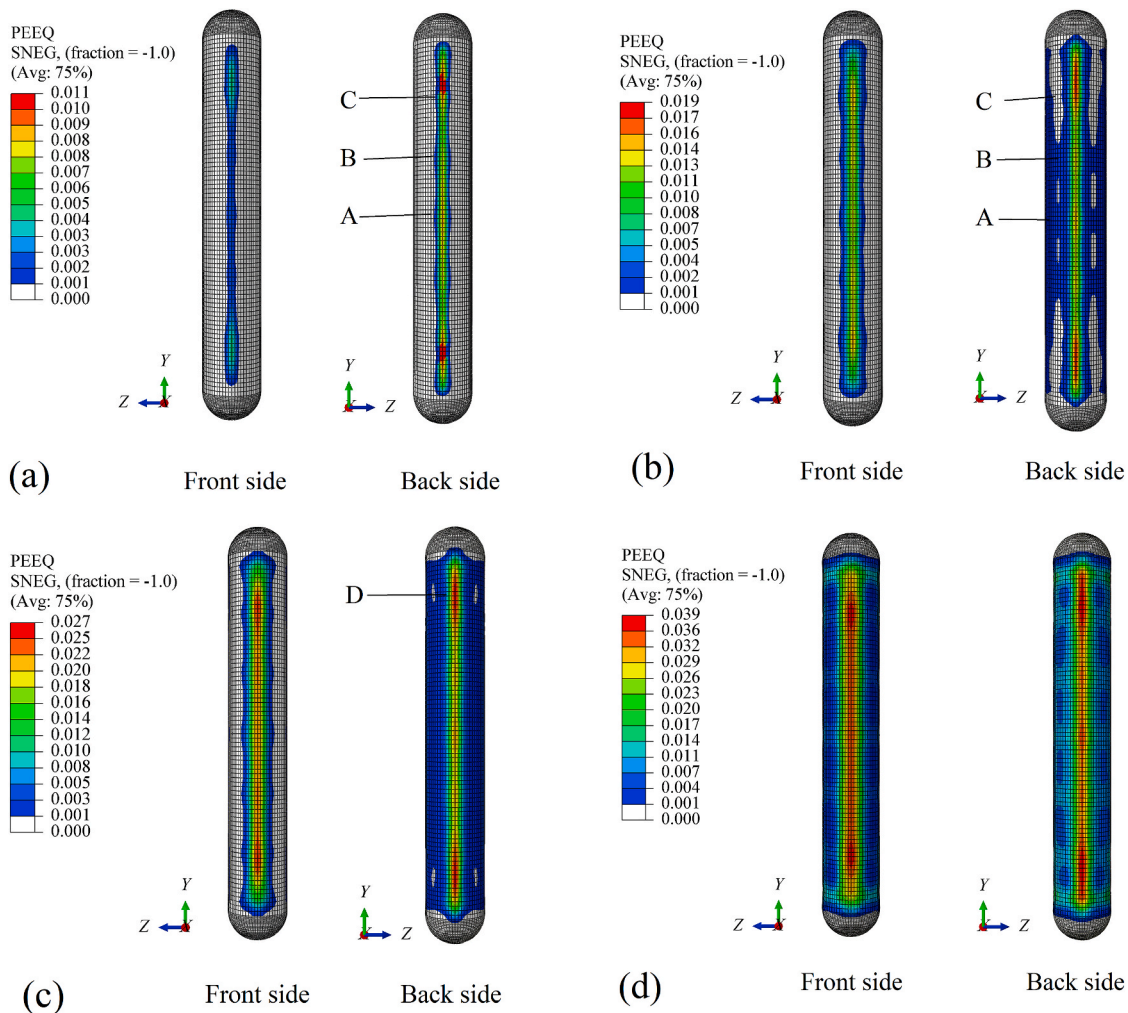
Fig. 18. Equivalent plastic strain of Model C subjected to UNEX shocks of different intensities: (a), (b), (c), and (d) are for Cases 12, 13, 14, and 15, respectively; the side depicted as the front-side is the one facing the explosion source.
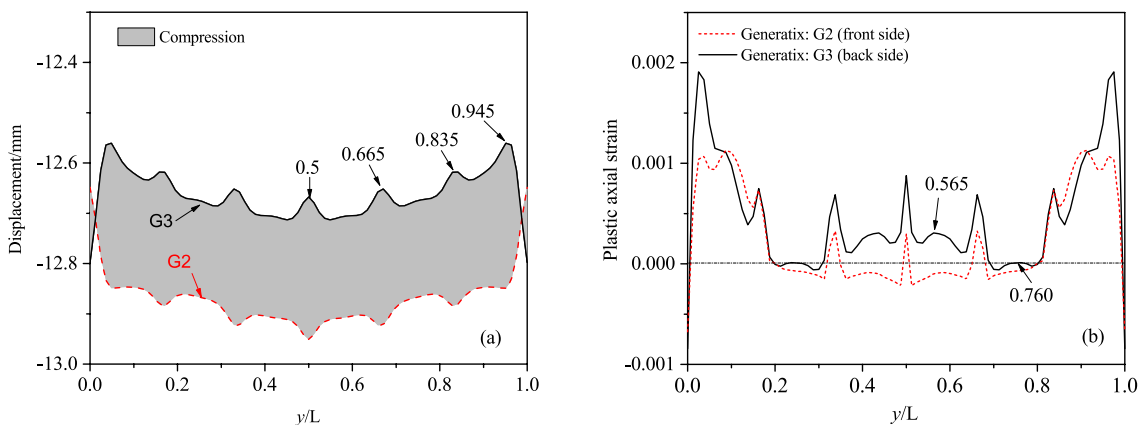

Fig. 19. Displacement and plastic strain along G2 and G3 of Case 14: (a) displacement; (b) axial plastic strain.
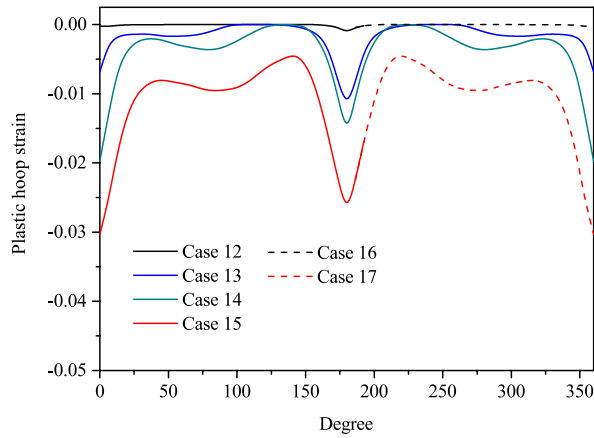
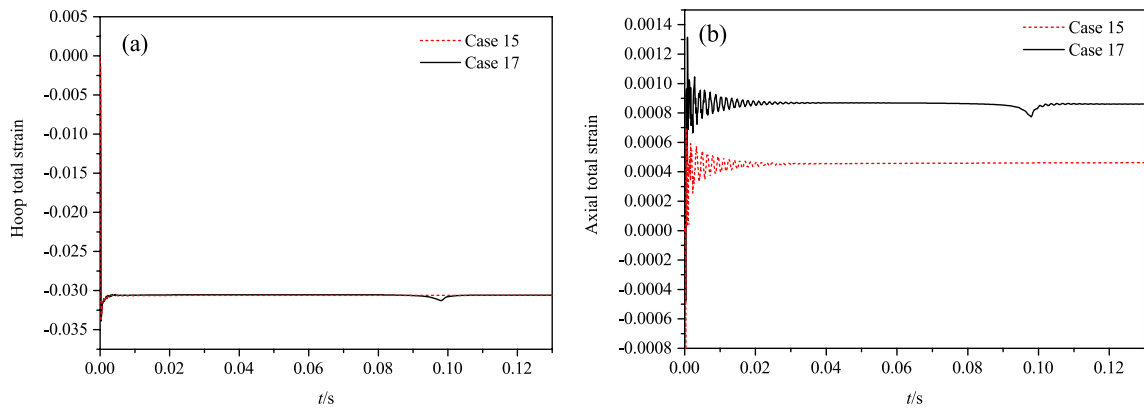**Fig. 20.** Plastic hoop strain along contour C3 of Model C.

Fig. 21. Time history of total strains at the nearest point for Cases 15 and 17: (a) total hoop strain; (b) total axial strain.
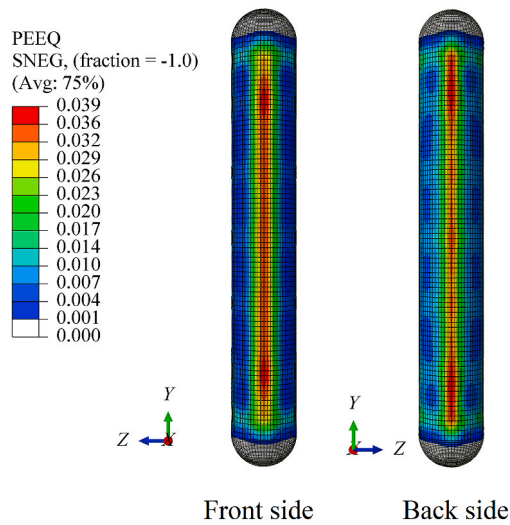

Fig. 22. Equivalent plastic strain of Model C for Case 17.

pressure on the hoop strain is negligible. In contrast, it has a remarkable effect on the axial strain, as shown in Fig. 21(b). It is noteworthy that the positive axial strain results from the hoop compression. Moreover, the axial strain is significantly less than the hoop strain; therefore, it could not alter the buckling mode, a fact that can be confirmed by comparing Figs. 22 and 18(a).

6. Discussion and conclusion

Cylindrical shells are one of the most commonly adopted elements in marine structures, ranging from small-size pipes to various containers and large submarines. Plastic buckling of shells could be caused by a UNEX load generated by an industrial accident or a hostile attack. The non-dimensional hull shock factor (HSF_P, which reflects the resilience of the material to an explosion), slenderness ratio *L/D*, and localised ring stiffener and endcap are factors that have an influence on the dynamic buckling modes. The dynamic buckling of three shells struck by a side-on UNEX shock with different HSF_P values was investigated. Models A and B, both sealed off by a flat plate at the ends, had an *L/D* of 3.2, whereas Model C, sealed off by hemispherical shells at the ends, had a larger *L/D* of 7.0. Models A and C were cylindrical shells without stiffeners, while Model B had a ring stiffener at its middle section.

The dynamic responses of shells subjected to a side-on UNEX shock were dominated by the dynamic buckling due to the side-on compression effect. Four typical hoop buckling modes existed, depending on the competition between the back-side and front-side buckling. They were i) back-side buckling, ii) back- and front-side buckling with dominant buckles at the back-side, iii) back- and front-side buckling with dominant buckles at the front side, and iv) overall buckling with very large buckles at the front-side originating from the priority buckling modes. Axial buckling modes could be categorised into global axial buckling modes with uniform spacing between the buckles and localised axial modes near the endcap or stiffener.

The hoop buckling modes could be significantly influenced by HSF_P; however, they are insensitive to *L/D*, ring stiffener, or endcap. The front-side buckling was caused by the shock transmitted from the fluid, while the back-side buckling could be attributed to the striking by the structural hoop stress waves at the back-side, which would propagate from the front-side along the circumferential direction. When HSF_p was small enough such that the front-side could withstand by only elastic deformation, the back-side buckling was dominant. In contrast, the front-side buckling was dominant when HSF_p was large; thus, energy could be consumed by the front-side buckling, resulting in weak structural hoop stress waves and subsequent back-side buckling.

A global axial buckling mode could be triggered on a shell with a large *L/D*. It consisted of primary and potential buckles alternating in the axial direction. The localised axial modes caused by the endcap or stiffener could cover the entire shells with a small *L/D*, resulting in no space for the development of the global axial buckling mode. The ring stiffener could mitigate the hoop plastic deformation and inhibit the growth of the priority hoop buckling modes around the stiffener. The endcap caused the inhomogeneous resistance of the shell to hoop compression along the axial direction. For a hard endplate, the reverse rotation motion due to the asymmetric tension provided by the front- and back-sides could lead to a localised axial compression of the front side. Generally, the impact of the ring stiffener and endcap on the axial buckling modes were localised.

Declaration of competing interest

The authors declare that they have no known competing financial interests or personal relationships that could have appeared to influence the work reported in this paper.

Acknowledgement

References

[1] Zhang J, Zhang M, Cui WC, Tang WX, Wang F, Pan BB. Elastic-plastic buckling of deep sea spherical pressure hulls. Mar Struct 2018;57:38–51.
[2] Wagner HNR, Hühne C, Zhang J, Tang W, Khakimova R. Geometric imperfection and lower-bound analysis of spherical shells under external pressure. Thin-Walled Struct 2019;143:106195.
[3] Zingoni, Enoma N. Strength and stability of spherical-conical shell assemblies under external hydrostatic pressure. Thin-Walled Struct 2020;146:106472.
[4] Muttaqie T, Park SH, Sohn JM, Cho SR, Nho IS, Han S, Cho YS. Implosion tests of aluminium-alloy ring-stiffened cylinders subjected to external hydrostatic pressure. Mar Struct 2021;78:102980.
[5] Lindberg HE, Florence AL. Dynamic pulse buckling: theory and experiment. Martinus Nijhoff Publishers; 1987.
[6] Kubiak T. Static and dynamic buckling of thin-walled plate structures. Springer; 2013.
[7] Huang YQ, Fu JY, Liu AR. Dynamic instability of Euler-Bernoulli nano-beams subject to parametric excitation. Compos B Eng 2019;164:226–34.
[8] Singha MK, Daripa R. Nonlinear vibration and dynamic stability analysis of composite plates. J Sound Vib 2009;328:541–54.
[9] Fu YM, Wang JZ, Mao YQ. Nonlinear analysis of buckling, free vibration and dynamic stability for the piezoelectric functionally graded beams in thermal environment. Appl Math Model 2012;36(9):4324–40.
[10] Pavlovic I, Pavlovic R, Ciric I, Karlicic D. Dynamic stability of nonlocal Voigt-Kelvin viscoelastic Rayleigh beams. Appl Math Model 2015;39(22):6941–50.
[11] Bitter NP, Shepherd JE. Dynamic buckling and fluid-structure interaction of submerged tubular structures, Blast Mitigation-Experimental and Numerical Studies. New York: Springer; 2014.
[12] Mustafa B, Al-Hassani STS, Reid SR. Axisymmetric dynamic buckling of submerged cylindrical shells. Comput Struct 1993;47(3):399–405.
[13] Florence AL and Abrahamson GR. A theory for critical loads to damage a cylindrical shell by large underwater explosion. Technical Report DNA 001-72-C-087 1976.

[14] Ren SF, Song Y, Zhang AM, Wang SP, Li PB. Experimental study on dynamic buckling of submerged grid-stiffened cylindrical shells under intermediate-velocity impact. Appl Ocean Res 2018;74:237–45.

[15] Cole RH. Underwater explosions. New York: Dover Publications; 1965.

[16] Klaseboer E, Hung KC, Wang C, Wand CW, Khoo BC, Boyce P, Debono S, Charlier H. Experimental and numerical investigation of the dynamics of an underwater explosion bubble near a resilient/rigid structure. J Fluid Mech 2005;537:387–413.

[17] Zhang AM, Liu YL. Improved three-dimensional bubble dynamics model based on boundary element method. J Comput Phys 2015;294:208–23.

[18] Zhang AM, Yang WS, Huang C, Ming FR. Numerical simulation of column charge underwater explosion based on SPH and BEM combination. Comput Fluid 2013;71:169–78.

[19] Li T, Zhang AM, Wang SP, Li S, Liu WT. Bubble interactions and bursting behaviors near a free surface. Phys Fluids 2019;31:042104.

[20] Jin Z, Yin C, Chen Y, Hua HX. Dynamics of an underwater explosion bubble near a sandwich structure. J Fluid Struct 2019;86:247–65.

[21] Geers TL, Hunter KS. An integrated wave-effects model for an underwater explosion bubble. J Acoust Soc Am 2002;111(4):1584–601.

[22] Geers TL, Park CK. Optimization of the g&h bubble model. Shock Vib 2005;12(1):3–8.

[23] Geers TL, Toothaker BJ. Third-order doubly asymptotic approximations for computational acoustics. J Comput Acoust 2000;8(1):101–20.

[24] Donea J, Giuliani S, Halleux JP. An arbitrary Lagrangian-eulerian finite element method for transient dynamic fluid-structure interactions. Comput Methods Appl Mech Eng 1982;33(1):689–723.

[25] Zong G. Dynamic plastic response of a submerged free-free beam to an underwater gas bubble. Acta Mech 2003;161:179–94.

[26] Zhang AM, Ren SF, Li Q, Li J. 3d numerical simulation on fluid-structure interaction of structure subjected to underwater explosion with cavitation. Appl Math Mech 2012;33:1191–206.

[27] Zong Z, Zhao YJ, Li HT. A numerical study of whole ship structural damage resulting from close-in underwater explosion shock. Mar Struct 2013;31:24–43.

[28] Wang J, Guo J, Yao XL, Zhang AM. Dynamic buckling of stiffened plates subjected to explosion impact loads. Shock Waves 2017;27(1):1–16.

[29] Zhao Q, Li Y, Chang B. Numerical study on the explosive effect of RDX-based aluminized explosives on stiffened plates. J Kor Phys Soc 2019;74(5):481–7.

[30] Ergin A. The response behavior of a submerged cylindrical shell using the Doubly Asymptotic Approximation method (DAA). Comput Struct 1997;62(6):1025–34.

[31] Praba RPS, Ramajeyathilagam K. Numerical investigations on the large deformation behaviour of ring stiffened cylindrical shell subjected to underwater explosion. Appl Ocean Res 2020;101:102262.

[32] Gong SW. Transient response of stiffened composite submersible hull to underwater shock and bubble. Compos Struct 2019;213:243–51.

[33] Brochard K, Sourne HL, Barras G. Estimation of the response of a deeply immersed cylinder to the shock wave generated by an underwater explosion. Mar Struct 2020;72:102786.

[34] Zhang N, Zong Z, Zhang WP. Dynamic response of a surface ship structure subjected to an underwater explosion bubble. Mar Struct 2014;35:26–44.

[35] Nie BC, Li JC, Zhang HQ. On the regimes of underwater explosion for a submerged slender structure by pulsating bubble. Mar Struct 2015;44:85–100.

[36] Xiao W, Zhang AM, Wang SP. The whipping response of a fluid filled cylindrical shell subjected to an underwater explosion. Mar Struct 2017;52:82–93.

[37] Zhou HC, Kong XS, Wang YW, Zheng C, Pei ZY, Wu WG. Dynamic response of hull girder subjected to combined underwater explosion and wave induced load. Ocean Eng 2021;235:109436.

[38] Kwon YW, Fox PK. Underwater shock response of a cylinder subjected to a side-on explosion. Comput Struct 1993;48:637–46.

[39] Li LJ, Jiang WK, Ai YH. Experimental study on dynamic response and shock damage of cylindrical shell structures subjected to underwater explosion. J Offshore Mech Arctic Eng 2011;133:011102.

[40] Gannon L. Submerged aluminum cylinder response to close-proximity underwater explosions – a comparison of experiment and simulation. Int J Impact Eng 2019;133:103339.

[41] Gupta S, Matos H, LeBlanc JM, Shukla A. Shock initiated instabilities in underwater cylindrical structures. J Mech Phys Solid 2016;95. 188–122.

[42] DeNardo N, Pinto M, Shukla A. Hydrostatic and shock-initiated instabilities in double-hull composite cylinders. J Mech Phys Solid 2018;120:96–116.

[43] Liang C-C, Tai Y-S. Shock responses of a surface ship subjected to noncontact underwater explosions. Ocean Eng 2006;33:748–72.

[44] Joubert PN. Some aspects of submarine design part 1. Hydrodynamics. DTIC Document; 2004. Technical report.

[45] Kyriakides S, Corona E. Mechanics of offshore pipelines vol. I buckling and collapse. Elsevier; 2017.

[46] Ahyi AC, Pernod P, Gatti O, Latard V, Merlen A, Überall H. Experimental demonstration of the pseudo-Rayleigh (a0) wave. J Acoust Soc Am 1998;104(5):2727–32.